Quantitative Analysis of Meteorite Elements Based on the Multidimensional Scaling–Back Propagation Neural Network Algorithm Combined with Raman Mapping-Assisted Micro-Laser Induced Breakdown Spectroscopy

Hongpeng Wang [1,4,†], Yingjian Xin [1,3,†], Peipei Fang [1,2,3], Yian Wang [2,3], Mingkang Duan [1,3] and Wenming Wu [5], Ruidong Yang [6], Sicong Liu [4], Liang Zhang [1,*] and Xiong Wan [1,2,*]

[1] Key Laboratory of Space Active Opto-Electronics Technology of the Chinese Academy of Sciences, Shanghai Institute of Technical Physics, Chinese Academy of Sciences, Shanghai 200083, China; 2010965@tongji.edu.cn (H.W.); simpson@mail.ustc.edu.cn (Y.X.); fangpeipei20@mails.ucas.ac.cn (P.F.); duanmingkang22@mails.ucas.ac.cn (M.D.)

[2] Key Laboratory of Systems Health Science of Zhejiang Province, School of Life Science, Hangzhou Institute for Advanced Study, University of Chinese Academy of Sciences, Hangzhou 310024, China fangpeipei20@mails.ucas.ac.cn (P.F.); wangyian22@mails.ucas.ac.cn (Y.W.); wanxiong@mail.sitp.ac.cn (X.W.)

[3] University of the Chinese Academy of Sciences, Beijing 100049, China; simpson@mail.ustc.edu.cn (Y.X.); fangpeipei20@mails.ucas.ac.cn (P.F.); wangyian22@mails.ucas.ac.cn (Y.W.); duanmingkang22@mails.ucas.ac.cn (M.D.)

[4] College of Surveying and Geo-Informatics, Tongji University, Shanghai 200092, China; sicong.liu@tongji.edu.cn

[5] Geological Brigade 105, Bureau of Geology and Mineral Exploration and Development of Guizhou Province, Guiyang 550018, China; wenmingwu84@163.com (W.W.);

[6] College of Resources and Environmental Engineering, Guizhou University, Guiyang 550025, China; rdyang@gzu.edu.cn (R.Y.)

* Correspondence: zhliang@mail.sitp.ac.cn (L.Z.); wanxiong@mail.sitp.ac.cn (X.W.)

† These authors contributed equally to this work.

Table S1 Chemical composition reference of certified reference materials (in wt%)

No.	Reference ID	Material	Fe	Mg	Na
A1	GBW03101a	Clay	7.385	0.276	0.045
A2	GBW03115	Soft clay	0.602	0.18	1.291
A3	GBW07127	Carbonate rock	0.1351	4.056	0.016
A4	GBW03121a	Kaolin	1.05	0.0414	0.033
A5	GBW07105(GSR-3)	Basalt	9.38	4.662	2.508
A6	GBW07125	Pegmatite	0.168	0.078	1.187
A7	GBW07217a	Dolomite	0.1568	12.222	0.017
A8	GBW07104(GSR-2)	Andesite	3.43	1.032	2.864
A9	GBW07121(GSR-14)	Granitic gneiss	2.184	0.978	3.932
A11	GBW03104	Shale	3.969	0.402	0.148
B1	GBW07106(GSR-4)	Quartz sandstone	2.254	0.0492	0.045
B2	GBW07108(GSR-6)	Argillaceous limestone	1.764	3.114	0.059
B3	GBW07163(GSO-2)	Polymetallic ore	8.4	0.834	0.178
B4	GBW07309(GSD9)	Namucuo sediments	3.402	1.434	1.068
B5	GBW07377(GSD-26)	Namucuo sediments, Tibet	3.612	1.038	0.616
B6	GBW07390(GSS-34)	Floodplain sediment	4.032	1.596	1.150
B7	GBW07405(GSS-5)	Yellow-red soil	8.834	0.366	0.089
B8	GBW07407(GSS-7)	Latosol	13.132	0.156	0.059
B10	GBW07447(GSS-18)	Saline alkali soil in Hangjinhou banner, Inner Mongolia	2.541	1.548	2.263
B11	GBW07449(GSS-20)	Saline alkali soil in Shanshan, Xinjiang	2.884	1.788	6.670
B12	GBW07450(GSS-21)	Lime calcium soil in Shihezi City, Xinjiang	2.849	1.224	1.499
B13	GBW07453(GSS-24)	Yangjiang Nanhai beach sediment	3.479	0.696	0.616
C1	GBW03123	Wollastonite	0.07	0.57	0.039

C2	GBW03125	Nepheline syenite	0.231	0.552	9.341
C3	GBW03107a	Limestone	0.406	1.074	0.020
D3	GBW07103(GSR-1)	Granite	1.498	0.252	2.322
D4	GBW07107(GSR-5)	Shale	5.32	1.206	0.260
D5	GBW07146	Nickel ore	7.497	8.736	1.180
D6	GBW07162(GSO-1)	Polymetallic lean ore	4.67	0.93	0.505
D7	GBW07164(GSO-3)	Copper rich silver ore	11.4	1.398	0.401
D8	GBW07165(GSO-4)	Lead zinc rich ore	13.72	0.354	0.022
D9	GBW07235	Lead ore	3.059	0.972	1.195
D10	GBW07236	Lead ore	2.653	1.236	0.049
D11	GBW07239	Molybdenum ore	10.262	1.098	0.571

According to cluster analysis, all spectra within the Raman mapping scanning area are classified into three categories, with 7 detection points defined as sample 1, 3180detection points defined as sample 2, and 944 detection points defined as sample 3.

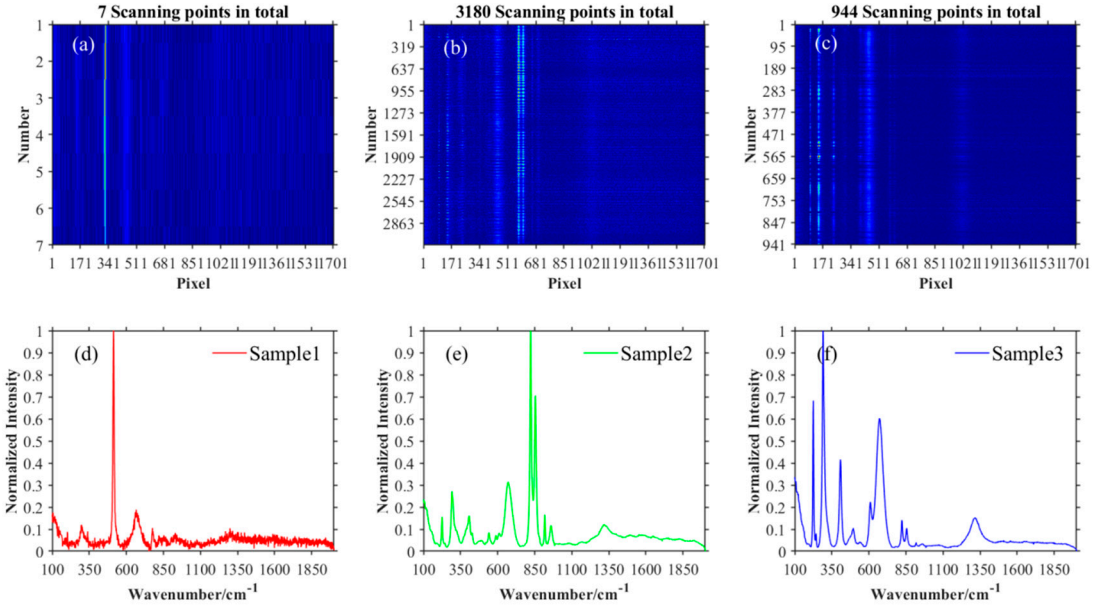

Figure S1 Three types of substances identified and their Raman spectra. (a) Detector response of Raman signals at 7 detection points; (b) Detector response of Raman signals at 3180 detection points; (c) Detector response of Raman signals at 944 detection points; (d) Average Raman spectra of 7 detection points; (e) Average Raman spectra of 3180 detection points; (f) Average Raman spectra of 944 detection points.

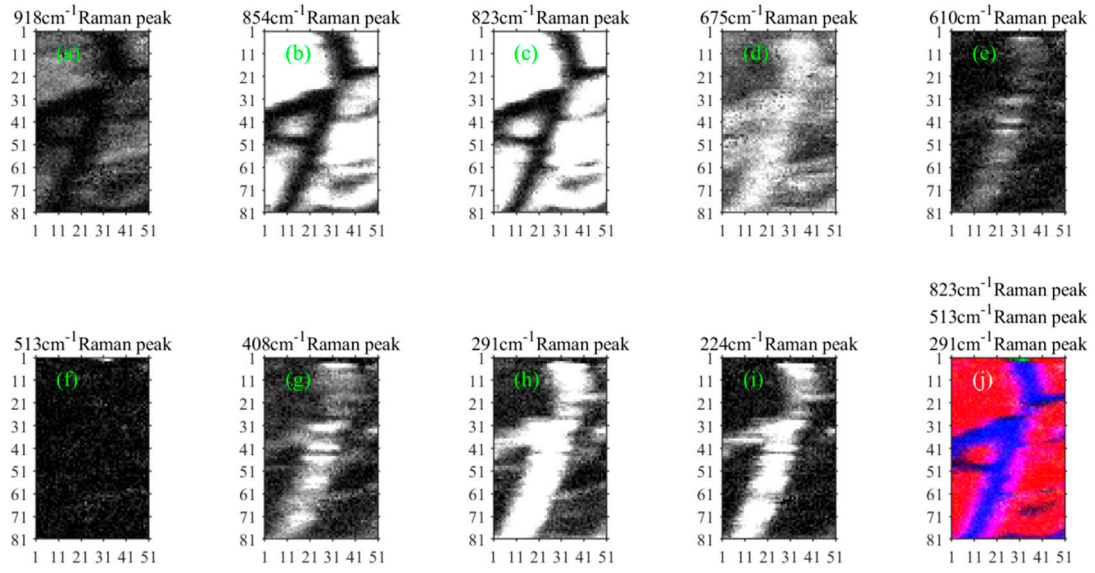

Figure S2 Mapping of different Raman peaks. (a) Mapping of Raman peaks at 918 cm^{-1}; (b) Mapping of Raman

peaks at 854 cm^{-1}; (c) Mapping of Raman peaks at 823 cm^{-1}; (d) Mapping of Raman peaks at 675 cm^{-1}; (e) Mapping of Raman peaks at 610 cm^{-1}; (f) Mapping of Raman peaks at 513 cm^{-1}; (g) Mapping of Raman peaks at 408 cm^{-1}; (h) Mapping of Raman peaks at 291 cm^{-1}; (i) Mapping of Raman peaks at 224 cm^{-1}; (j) Pseudo-color composite images of Raman peaks at wave numbers 823 (R channel), 513 (G channel), and 291 (B channel) cm^{-1}.

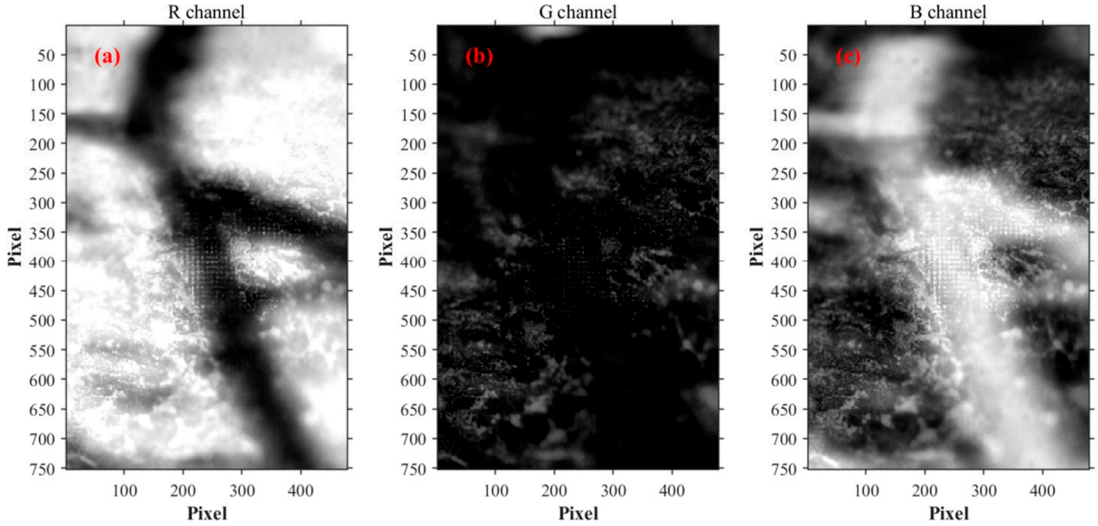

Figure S3 The gray-scale images of three channels. (a) Mapping of intensities of Raman peak at 823 cm^{-1}(typical Raman peaks of sample 2); (b) Mapping of intensities of Raman peak at 513 cm^{-1}(typical Raman peaks of sample 1); (c) Mapping of intensities of Raman peak at 291 cm^{-1}(typical Raman peaks of sample 3).

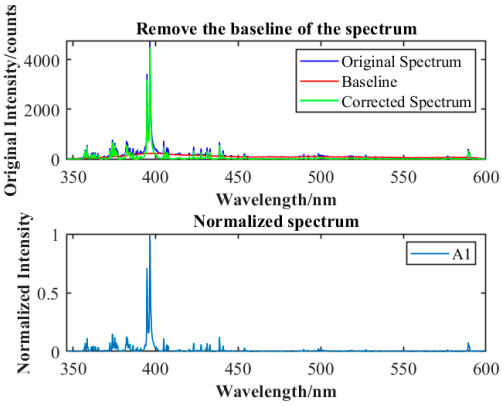

Figure S4 Spectral data preprocessing of A1

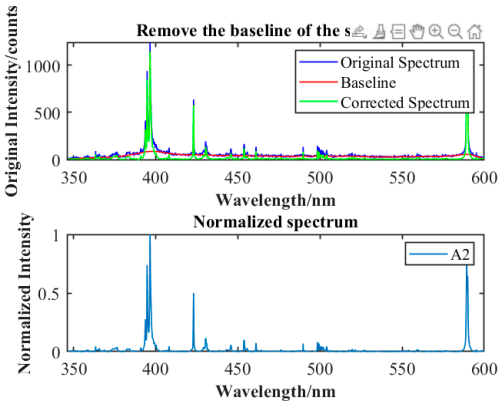

Figure S5 Spectral data preprocessing of A2

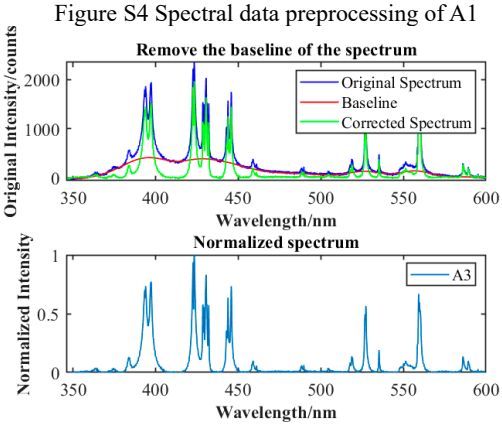

Figure S6 Spectral data preprocessing of A3

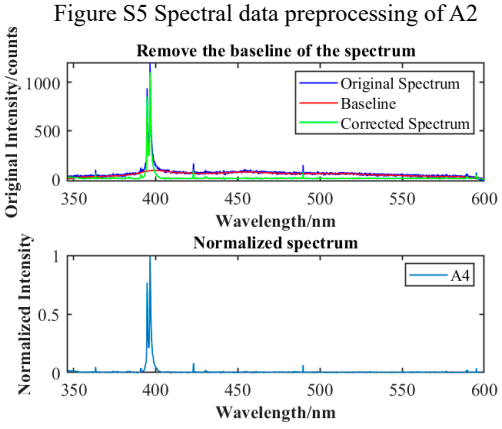

Figure S7 Spectral data preprocessing of A4

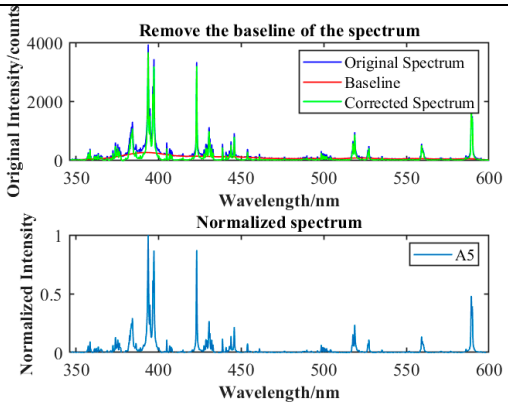

Figure S8 Spectral data preprocessing of A5

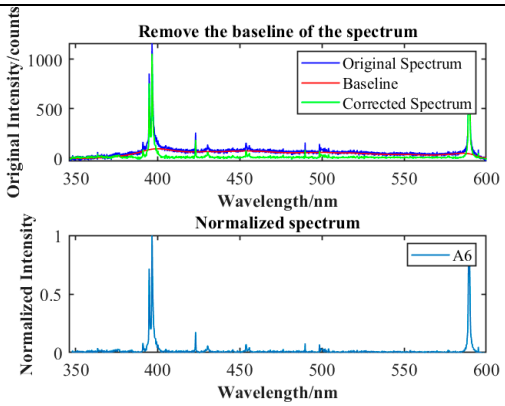

Figure S9 Spectral data preprocessing of A6

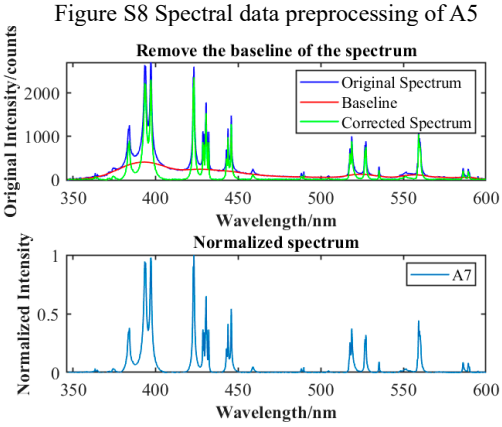

Figure S10 Spectral data preprocessing of A7

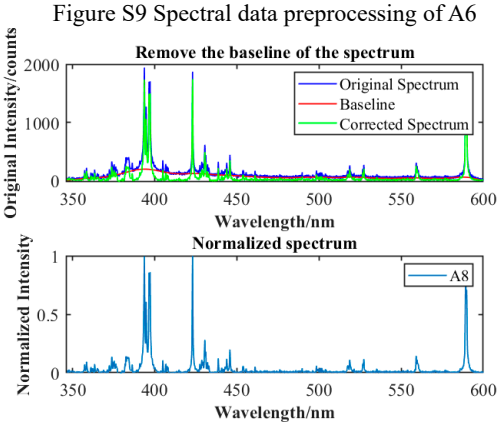

Figure S11 Spectral data preprocessing of A8

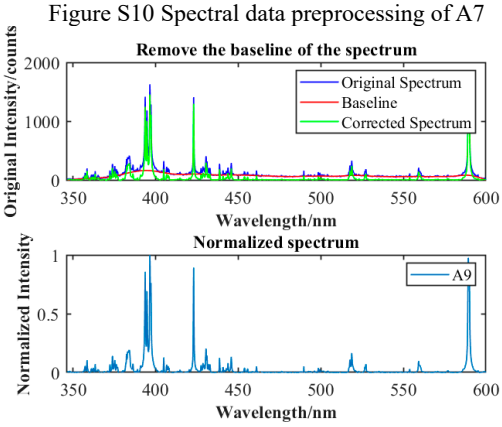

Figure S12 Spectral data preprocessing of A9

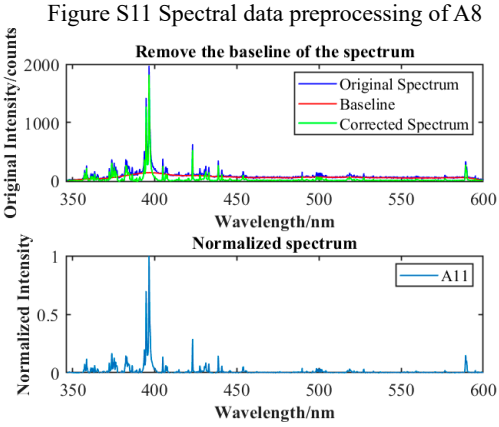

Figure S13 Spectral data preprocessing of A11

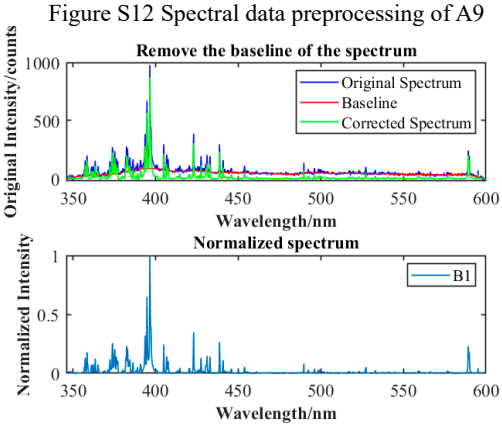

Figure S14 Spectral data preprocessing of B1

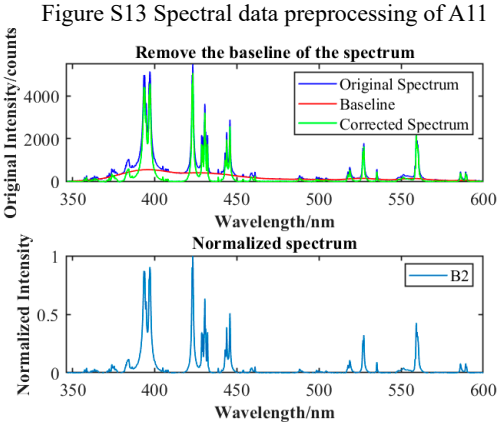

Figure S15 Spectral data preprocessing of B2

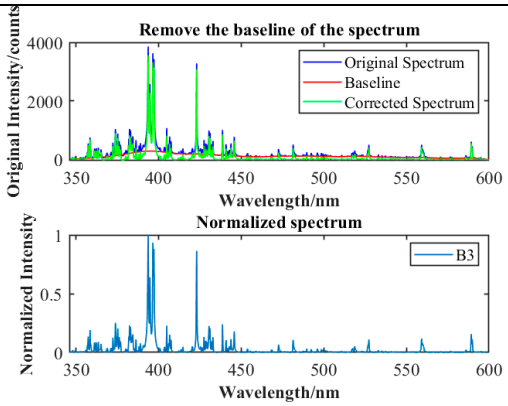

Figure S16 Spectral data preprocessing of B3

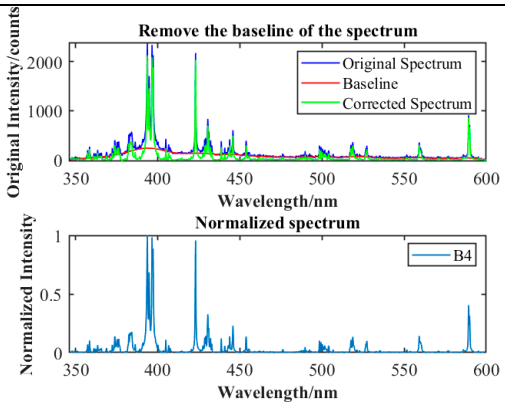

Figure S17 Spectral data preprocessing of B4

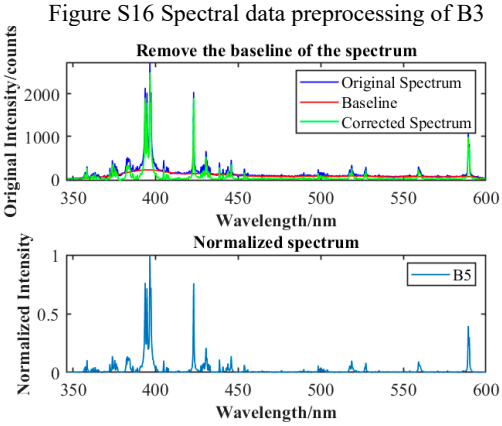

Figure S18 Spectral data preprocessing of B5

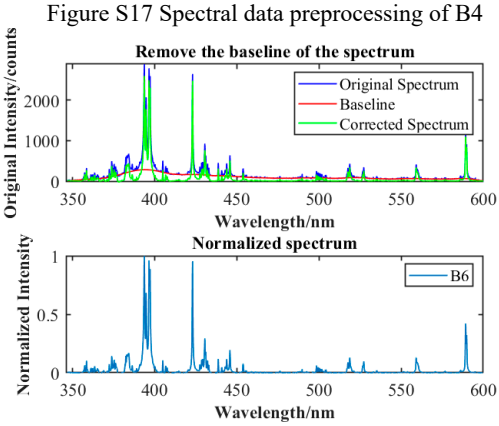

Figure S19 Spectral data preprocessing of B6

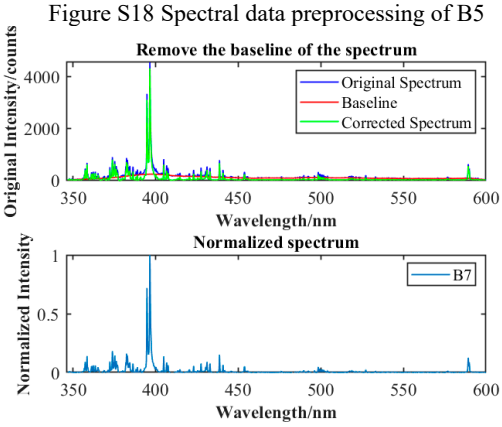

Figure S20 Spectral data preprocessing of B7

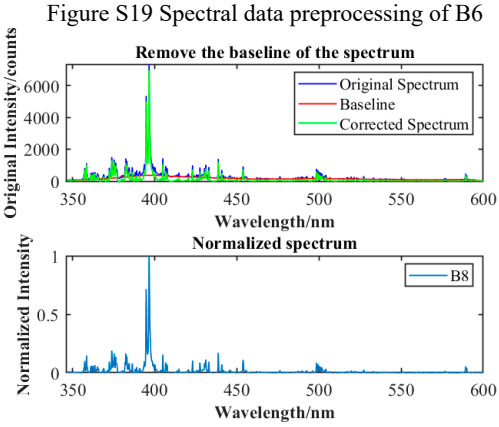

Figure S21 Spectral data preprocessing of B8

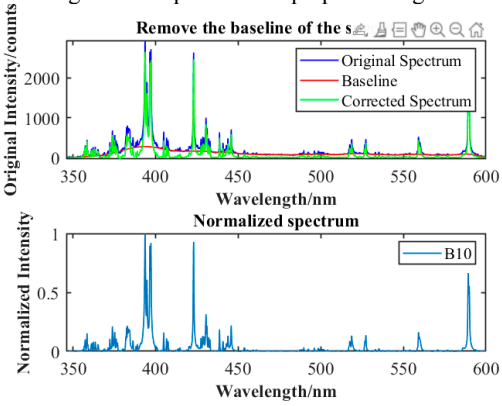

Figure S22 Spectral data preprocessing of B10

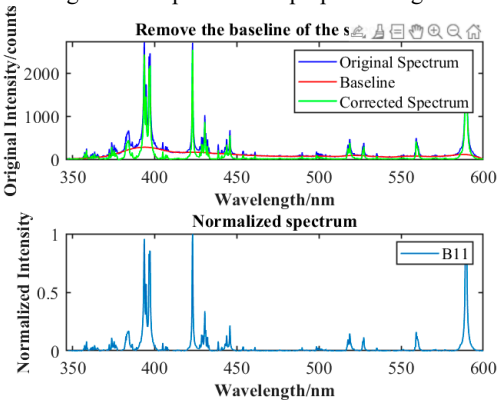

Figure S23 Spectral data preprocessing of B11

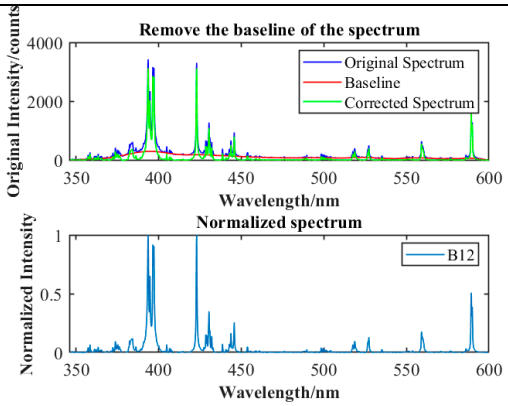

Figure S24 Spectral data preprocessing of B12

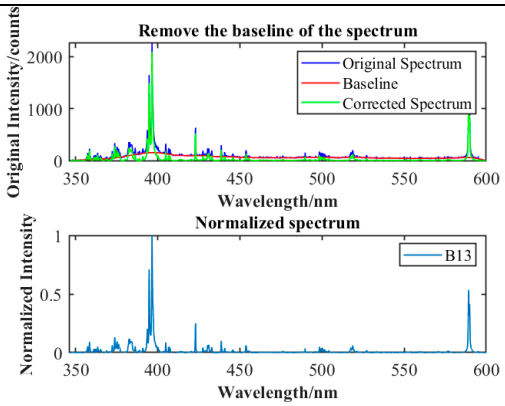

Figure S25 Spectral data preprocessing of B13

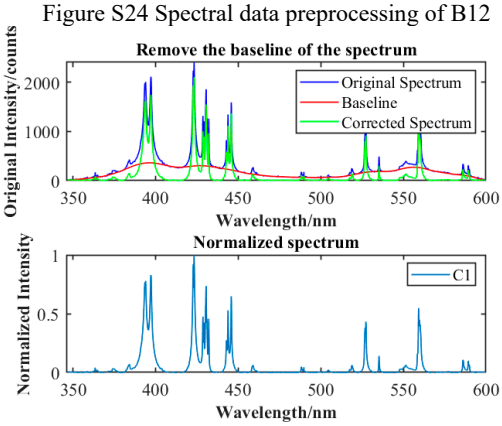

Figure S26 Spectral data preprocessing of C1

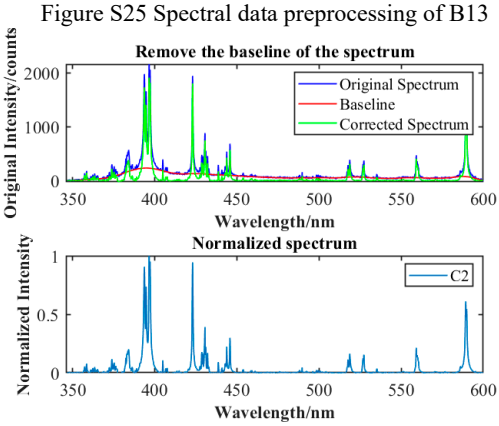

Figure S27 Spectral data preprocessing of C2

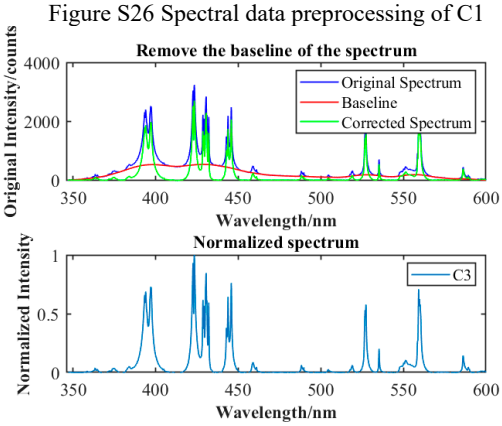

Figure S28 Spectral data preprocessing of C3

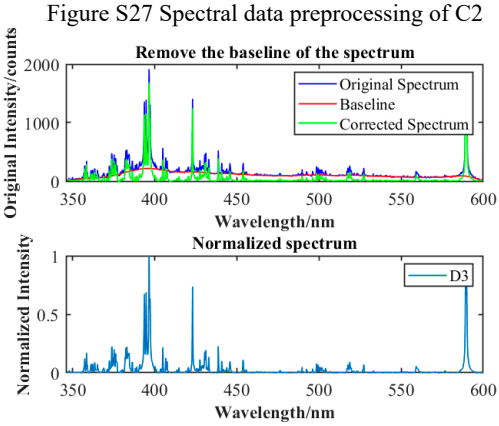

Figure S29 Spectral data preprocessing of D3

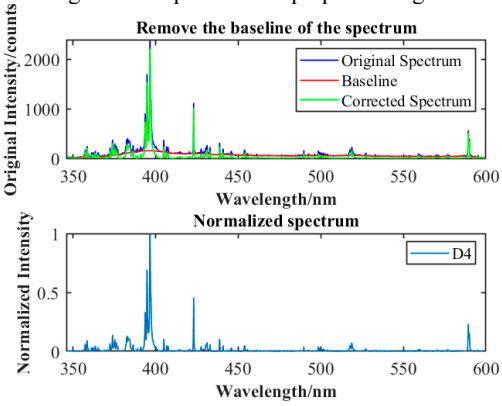

Figure S30 Spectral data preprocessing of D4

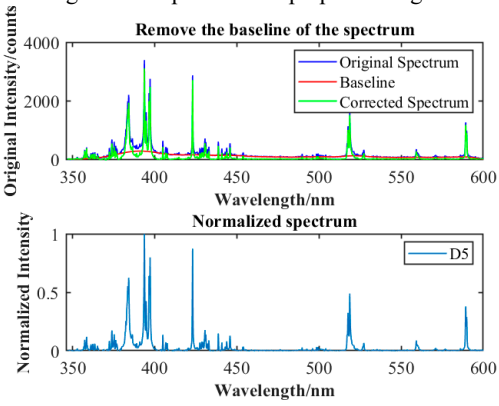

Figure S31 Spectral data preprocessing of D5

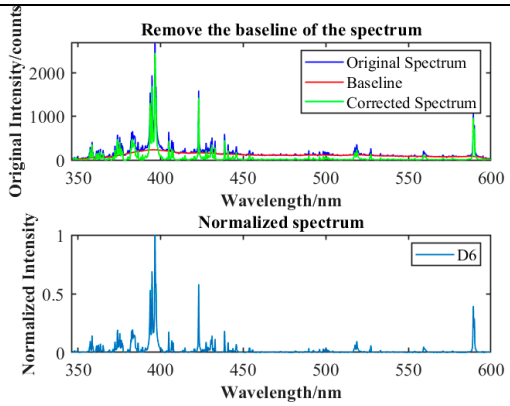

Figure S32 Spectral data preprocessing of D6

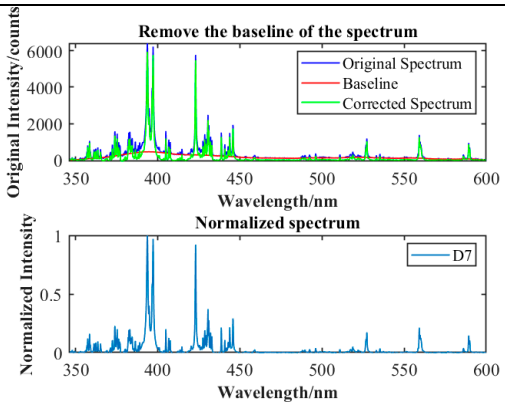

Figure S33 Spectral data preprocessing of D7

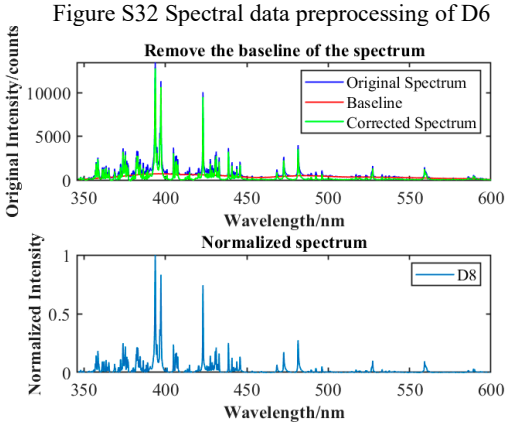

Figure S34 Spectral data preprocessing of D8

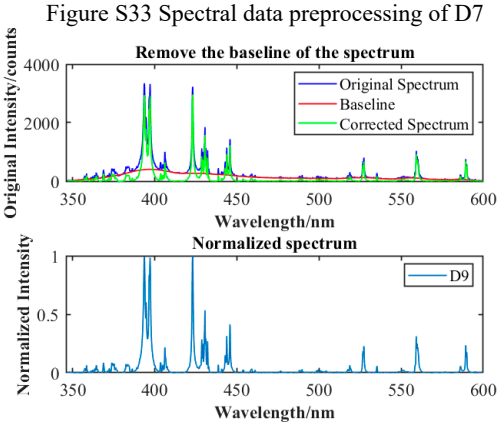

Figure S35 Spectral data preprocessing of D9

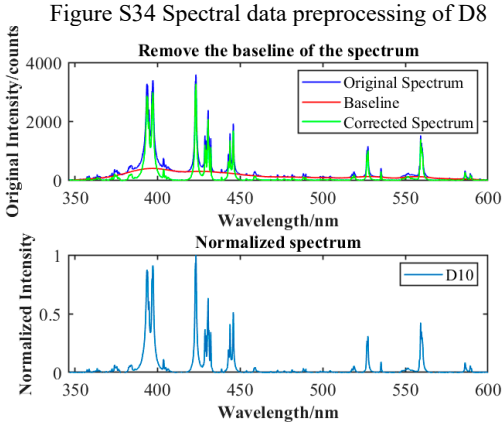

Figure S36 Spectral data preprocessing of D10

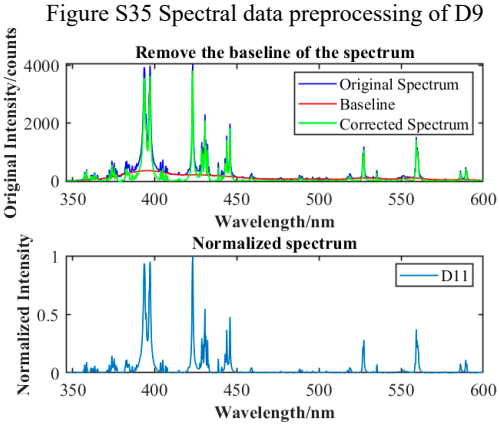

Figure S37 Spectral data preprocessing of D11